

A constitutive model for unsaturated soils with consideration of inter-particle bonding



Ran Hu^{a,b}, Hui-Hai Liu^c, Yifeng Chen^{a,b}, Chuangbing Zhou^{a,b,*}, Domenico Gallipoli^d

^a State Key Laboratory of Water Resources and Hydropower Engineering Science, Wuhan University, Wuhan 430072, China

^b Key Laboratory of Rock Mechanics in Hydraulic Structural Engineering (Ministry of Education), Wuhan University, Wuhan 430072, China

^c Earth Sciences Division, Lawrence Berkeley National Laboratory, Berkeley, CA 94720, USA

^d Laboratoire SIAME, Université de Pau et des Pays de l'Adour, France

ARTICLE INFO

Article history:

Received 27 July 2013

Received in revised form 8 March 2014

Accepted 9 March 2014

Available online 29 March 2014

Keywords:

Constitutive model

Unsaturated soils

Bonding effect

Water menisci

Plasticity

Critical state

ABSTRACT

The paper presents a physically-based constitutive model for unsaturated soils that considers the bonding effect of water menisci at inter-particle contacts. A bonding factor has been used to represent the magnitude of the equivalent bonding stress, defined as the bonding force per unit cross-sectional area. The average skeleton stress is employed to represent the effect of average fluid pressures within soil pores. Based on an empirical relationship between the bonding factor ζ and the ratio e/e_s (where e and e_s are void ratios at unsaturated and saturated states, respectively, at the same average skeleton stress), we propose an elasto-plastic constitutive model for isotropic stress states, and then extend this model to triaxial stress states within the framework of critical state soil mechanics. Because only one yield surface is needed in the proposed model, a relatively small number of parameters are required. Comparisons between experimental data and model results show that, in most cases, the proposed model can reasonably capture the important features of unsaturated soil behavior.

© 2014 Elsevier Ltd. All rights reserved.

1. Introduction

Modeling the stress–strain behavior of unsaturated soils is one of the greatest challenges of geotechnical engineering. It has long been recognized that Terzaghi's effective stress can be used to successfully describe the mechanical behavior of saturated soils. But for soils under unsaturated conditions, the characterization of deformation behavior is difficult, owing to the existence of bonding forces induced by water menisci between soil particles. This bonding force acts at the points of contact between soil particles [1–3] and complicates the description of the soil mechanical behavior. This bonding force has a significant effect on the mechanical behavior of unsaturated soils and is closely related to degree of saturation, suction and pore size distribution. Some investigators have attempted to use a single stress variable to describe the stress–strain relationship of unsaturated soils [4–6] while others have used two independent constitutive variables [9,10,7,8]. Two inde-

pendent constitutive variables are also used in the model presented in this paper.

In early elasto-plastic models, suction was commonly employed together with net stress to describe the mechanical behavior of unsaturated soils [11,1,12–14]. For example, Alonso et al. [11] assumed that normal compression lines are a function of suction and then derived the loading-collapse yield curve, which plays a central role in their model. The model is able to reproduce important features of unsaturated soils and has provided a basic framework for subsequent developments. For models of this kind, however, the capillary bonding effect of water menisci is measured by suction alone, which is not enough to properly describe real behavior.

Other elasto-plastic models have been proposed where the bonding effect is described by a constitutive variable which also includes degree of saturation [15–24]. Wheeler et al. [17] discussed the inter-relationships between the hydraulic and mechanical behavior in unsaturated soils emphasizing the role of the inter-particle forces associated to the water retention behavior. This bonding effect is also considered in a model by Buscarnera and Nova [23] that deals with mechanical instabilities in unsaturated soils. Recently, Zhou et al. [24] represented bonding and debonding effects in unsaturated soils by assuming that stiffness is a function of the effective degree of saturation.

* Corresponding author at: State Key Laboratory of Water Resources and Hydropower Engineering Science, Wuhan University, Wuhan 430072, China. Tel./fax: +86 27 68774295.

E-mail addresses: whuran@whu.edu.cn (R. Hu), hhlui@lbl.gov (H.-H. Liu), csyfchen@whu.edu.cn (Y. Chen), cbzhou@whu.edu.cn (C. Zhou), domenico.gallipoli@univ-pau.fr (D. Gallipoli).

To the best of our knowledge, Gallipoli et al. [25] were the first to consider the effect of capillary bonding within an elasto-plastic constitutive model. They used the variable, ξ , to describe the magnitude of the bonding exerted by inter-particle water menisci:

$$\xi = f(s) \cdot (1 - S_r) \quad (1)$$

where S_r is water saturation and the term $(1 - S_r)$ accounts for the number of water menisci per unit volume of solid fraction; the function $f(s)$ expresses the ratio of the inter-particle attraction at the two suctions of s and zero for the ideal case of a water meniscus located at the contact between two identical spheres. This leads to a unique relationship between the bonding variable ξ and the ratio e/e_s , where e and e_s are void ratios calculated at the same value of average skeleton stress under unsaturated and saturated conditions, respectively [25,26]. The model is capable of reproducing many important features of unsaturated soil behavior with a single yield surface and requires only a small number of model parameters under isotropic stress conditions. The definition of the bonding variable in the model of Gallipoli et al. [25] is derived from physical considerations of a qualitative nature rather than from a closed-form calculation of the bonding force. This paper presents a different approach to the definition of the bonding variable based on the explicit consideration of the solid–liquid–gas geometry at the inter-particle contact in order to rigorously calculate the bonding stress.

This work assumes an idealized soil consisting of identical, regularly distributed, spherical particles. This means that all pores have the same shape and dimension, though this shape and dimension can change with changing void ratio. This implies that, for values of degree of saturation smaller than one, pore water exists only in the pendular regime and the presence of bulk water is neglected for the definition of the capillary bonding factor. This is of course a simplification because real soils have pores of different sizes and, for values of degree of saturation smaller than one, there will be smaller pores filled with water (bulk water) and larger pores filled with air, with water menisci at inter-particle contacts (meniscus water). In real soils, bulk water will only disappear at very low values of degree of saturation.

Despite these simplifying assumptions, which are necessary to obtain a closed form expression of the bonding force, the paper provides a useful theoretical framework for comparison against experimental data and allows a rigorous quantification of capillary bonding between soil particles in the pendular regime for different values of void ratio.

To rigorously represent the effect of capillary bonding, we define the bonding stress as the bonding force divided by the area that the force acts on. Then, we propose a relationship between the ratio (e/e_s) and the bonding stress, and validate that relationship against a series of experimental data from isotropic and triaxial loading tests. After that, we develop a physically based constitutive model, with a single yield surface, for isotropic stress states and then extend that model to triaxial stress states. A number of different experimental data sets are used to evaluate the model.

2. The bonding factor

For calculating the bonding force due to inter-particle water menisci, we conceptualize the soil as consisting of identical spherical particles. Consider a water meniscus between two such soil particles (Fig. 1). The relationship between the radius of curvature of the air–water interface r and the shortest distance from the contact point B to the interface r_1 can be described by

$$(\beta r + R)^2 = R^2 + (r + r_1)^2 \quad (2)$$

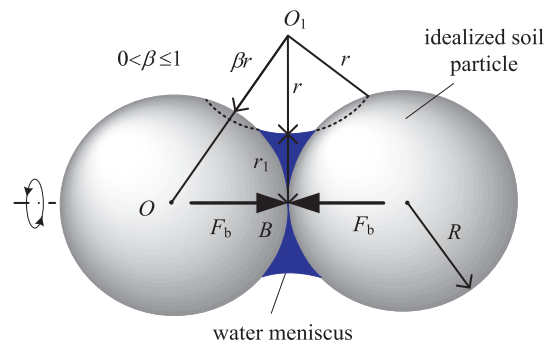


Fig. 1. Illustration of water meniscus between two identical contacting spheres.

where β is a parameter that decreases with increasing values of the contact angle ($\beta = 1$ for zero contact angle) and R is the radius of the idealized soil particles.

Unlike silt/sand/gravel particles, which have generally sub-rounded shapes, clay particles are flat and plate-like. Nevertheless, a clay compacted dry of optimum could still be represented as an assembly of aggregates of individual clay particles, where each aggregate is modeled as a sphere with an equivalent radius R [27] of the order of magnitude of $1 \mu\text{m}$ [25]. Along the same line, the clay soils are approximately represented by spheres in this study. In other words, the radius R in this study is referred as the average size of soil particles.

The capillary pressure, defined as the difference between pore air pressure and pore water pressure, is given by the Young–Laplace equation (e.g. [28]):

$$s \equiv p_a - p_w = T_s \left(\frac{1}{r} - \frac{1}{r_1} \right) \quad (3)$$

where p_a and p_w are the pore air pressure and pore water pressure (compression positive), respectively, and T_s is the surface tension of water. Note that $T_s = 0.0727 \text{ N/m}$ for a temperature of 20°C [29].

By neglecting gravity, the bonding force induced by the water meniscus in Fig. 1 can therefore be calculated as (e.g., [30,31])

$$F_b = \pi r_1^2 s + 2\pi r_1 T_s \quad (4)$$

Eq. (4) expresses the bonding force induced by water menisci. Note that there is another kind of the bonding force that is associated with clay mineralogy in the clayey soils, which does not closely relate to water menisci or the variation of saturation. Thus, we neglected the bonding stress associated with clay mineralogy in this study.

As previously indicated, our study is based on the assumptions that natural soils consist of identical soil particles approximated as spheres and the neglect of the bonding forces associated with clay mineralogy. Despite the limitations indicated above, Fig. 1 and the relevant equations provide a first approximation for soils, which leads to a simple and explicit expression of bonding stress. The reasonableness of our consideration was evaluated later by comparisons between model results and experimental data.

Substituting $\alpha = r_1/R$ into Eq. (2) yields

$$r = \begin{cases} \frac{\beta - \alpha - \sqrt{\alpha^2 \beta^2 + \beta^2 - 2\alpha\beta}}{1 - \beta^2} R, & \text{when } \beta < 1 \\ \frac{\alpha^2}{2(1 - \alpha)} R, & \text{when } \beta = 1 \end{cases} \quad (5)$$

Given that suction s must always be positive, α and β must meet the following condition:

$$0 \leq \alpha \leq \frac{2\beta}{4 - \beta^2} \quad (6)$$

and the meaningful range of α values therefore depends on the β value (i.e. it depends on the contact angle).

Note that Eq. (5) is obtained by solving a second order equation which has two solutions. Only one of these two solutions (that with the minus sign in front of the square root) is retained while the second one (that with the plus sign in front of the square root) is discarded. The second solution is discarded because, in order for suction to be positive, it would be necessary to impose a restriction on the values of α and β that results in a negative argument of the square root.

Substituting Eqs. (3) and (5) and $r_1 = \alpha R$ into Eq. (4) leads to

$$F_b = \pi RT_s \left(\beta + \sqrt{\alpha^2 \beta^2 + \beta^2 - 2\alpha\beta} \right) \quad (7)$$

Interestingly, the bonding force tends to a finite positive value when $r_1 \rightarrow 0$ (i.e. when $\alpha \rightarrow 0$) despite the cross-sectional area over which suction acts tends to zero. This is explained by inspection of Eq. (4), whose second term vanishes as $r_1 \rightarrow 0$ while the first term tends to a finite value due to the fact that $s \rightarrow +\infty$ when $r_1 \rightarrow 0$.

For different β values, the relationship between the normalized bonding force $F_b/(\pi RT_s)$ and α is shown in Fig. 2 (solid lines), indicating that the normalized bonding force varies from 2 to zero and decreases approximately linearly with α at a given value of β . Thus, the relationship of Eq. (7) can be approximated with a simpler linear expression:

$$F_b = \pi RT_s (2\beta - \beta_1 \alpha) \quad (8)$$

where $\beta_1 = \sqrt{2 - \beta^2}$. A comparison of the original Eq. (7) with the simpler linearized Eq. (8) is also shown in Fig. 2.

For a given particle packing, the equivalent bonding stress σ_b can then be estimated as

$$\sigma_b = F_b/S_b \quad (9)$$

where S_b is the cross-sectional area normal to the force direction (Fig. 3). As shown in Fig. 3, for simple cubic packing ($e = 0.91$), the force F_b spreads over an effective area $S_b = 4R^2$. For other packings, such as tetrahedral ($e = 1.95$), octahedral ($e = 0.47$) and dodecaedric ($e = 0.35$), the values of S_b are $16R^2/\sqrt{3}$, $4R^2/\sqrt{3}$, and $\sqrt{2}R^2$, respectively [32]. Previous research has investigated the effect of pore-scale on soil properties. For example, Willson et al. [33] conducted X-ray computed tomography (XCT) to quantitatively assess the particle- and pore-scale properties of fine Ottawa sand, while Likos and

Jaafar [34] introduced a pore-scale framework for modeling the water retention behavior of partially saturated granular materials.

In this work, the relationship between S_b and e is approximated by a quadratic fitting function [32]: $S_b = g(e)R^2 = (0.32e^2 + 4.06e + 0.11)R^2$. As a result, the equivalent bonding stress σ_b for different packing patterns is written as:

$$\sigma_b = \frac{\pi T_s (2\beta - \beta_1 \alpha)}{g(e)R} \quad (10)$$

The variable α in Eq. (10) is proportional to the one-fourth power of the degree of saturation [29,35], i.e. $\alpha = C \cdot (S_r)^{1/4}$ where C is a constant depending on particle packing. Substituting $\alpha = C \cdot (S_r)^{1/4}$ into Eq. (10) yields:

$$\sigma_b = \frac{\pi T_s (2\beta - C\beta_1 S_r^{1/4})}{g(e)R} \quad (11)$$

Obviously, the bonding effect of inter-particle water menisci vanishes at the saturated state, i.e. $\sigma_b = 0$ for $S_r = 1$. Thus, the variables C , β , and β_1 should meet the following condition:

$$C = 2\beta/\beta_1 \quad (12)$$

By Eqs. (11) and (12), the bonding stress σ_b can then be rewritten as:

$$\sigma_b = \frac{2\pi\beta T_s}{R} \cdot \frac{(1 - S_r^{1/4})}{g(e)} \quad (13)$$

The bonding stress σ_b is therefore expressed as the product of two factors, $2\pi\beta T_s R$ and $(1 - S_r^{1/4})/g(e)$. The first factor, $2\pi\beta T_s R$, depends on contact angle, surface tension, and mean particle radius. The contact angle depends on the characteristics of the solid-liquid interface, the surface tension depends on temperature, and the mean particle radius depends on soil type (note that the change of mean particle radius is far smaller than the change in pore volume during deformation [36]). Thus, the factor $2\pi\beta T_s R$ can be reasonably assumed to be constant during isothermal deformation.

The second factor $(1 - S_r^{1/4})/g(e)$ depends on degree of saturation and void ratio and represents the evolution of the bonding stress during isothermal deformation. Thus, we define the dimensionless term $(1 - S_r^{1/4})/g(e)$ as the bonding factor, ζ , directly related to the magnitude of the bonding stress, σ_b :

$$\zeta = \frac{1 - S_r^{1/4}}{g(e)} \quad (14)$$

It is of interest to compare the bonding factor given by Eq. (14) with that proposed by Gallipoli et al. [25]. Firstly, our bonding factor is derived based on the reasoning that bonding force exists for any two contacting soil particles under unsaturated conditions. However, Gallipoli et al. [25] considered that only a portion of contacting soil particles are subjected to bonding force under unsaturated condition and their fraction is equal to $1 - S_r$. Essentially, they assumed that contacting particles associated with pores filled with water have no bonding force even under unsaturated conditions. Based on current unsaturated flow theories [37,38], local equilibrium (that the same capillary pressures exist across all pores) holds, although water fills small pores first as a result of capillary effects. In other words, under unsaturated conditions, pore water from different pores has the same capillary pressure no matter whether they are completely filled or not. Therefore, a bonding force always exists between two contacting particles as long as suction exists.

Secondly, in this work the bonding factor is derived from a closed-form calculation of the bonding stress taking into account factors like particle packing, contact angle and degree of saturation. This provides a rigorous characterization of capillary bonding, which is again different from Gallipoli et al. [25] where a function

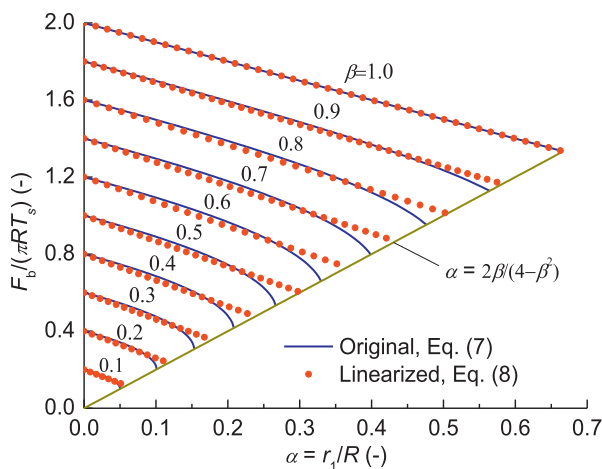


Fig. 2. Relationship between $F_b/(\pi RT_s)$ and α for different β values.

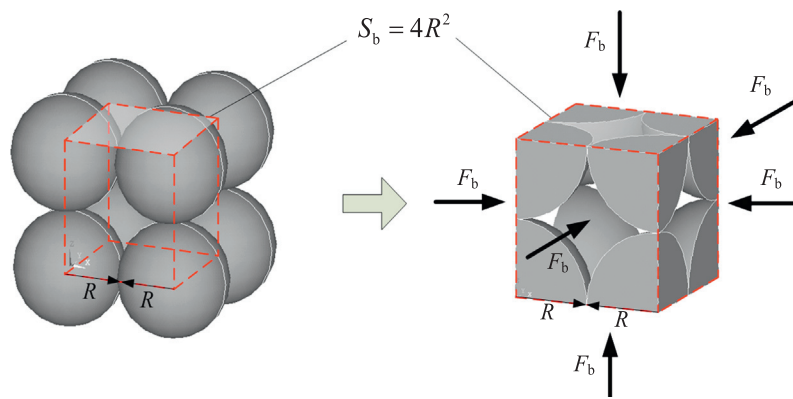


Fig. 3. Schematic view of the bonding force due to water menisci for cubic packing.

$f(s)$ is invoked to describe the variation of capillary bonding with suction without an explicit relation with the bonding stress. Whether $f(s)$ can be used for soil particles that are larger than $1 \mu\text{m}$ needs to be further investigated. Note that our closed-form expression of bonding factor is not limited by particle sizes.

Finally, the present paper presents a general constitutive model for triaxial stress states while the work of Gallipoli et al. [25] is only applicable to isotropic stress states. The present model is therefore able to reproduce the main features of unsaturated soil behavior under shearing. For example, the model can capture the development of irreversible shear strains during wetting under constant deviator stress as shown in Section 5.4.2.

3. Model assumptions

In the previous section, the bonding factor has been derived to represent the inter-particle bonding due to capillarity. In this section, we use this factor and the average skeleton stress to develop an empirical relationship describing the irreversible volumetric behavior of soils under both saturated and unsaturated states.

3.1. Stress variables

By extending Terzaghi's effective stress principle to the unsaturated state, the average skeleton stress is defined as [36]:

$$\sigma'_{ij} = (\sigma_{ij} - p_a \delta_{ij}) + S_r s \delta_{ij} \quad (15)$$

where σ'_{ij} is the average skeleton stress tensor, σ_{ij} is the total stress tensor, δ_{ij} is Kronecker delta and $\sigma_{ij} - p_a \delta_{ij}$ is the net stress tensor. The traces of the net stress tensor and average skeleton stress tensor are the mean net stress p_{net} , and the mean average skeleton stress, p' , respectively. Eq. (15) is obtained from the expression of Bishop's stress [39] if the weighting factor, χ , is replaced by the degree of saturation. As mentioned above, the bonding effect of water menisci cannot be fully captured by the average skeleton stress. That is why a single stress variable, as that of Eq. (15), cannot capture fundamental features of unsaturated soil behavior, including wetting-induced irreversible compression (at high confining stress), reversible swelling (at low confining stress) [40] and drying-induced irreversible compression during wetting–drying cycles [17]. In order to overcome such limitations, two constitutive variables, σ'_{ij} and ζ , are used in our model, where ζ is the bonding factor accounting for the presence of inter-particle water menisci.

3.2. The relationship between e/e_s and ζ

Two normally consolidated samples at the same average skeleton stress can have different void ratios, if their degrees of

saturation are different, because of the different action of water menisci in the two cases.

Using a methodology similar to that reported by Gallipoli et al. [25], we propose the following empirical relationship to describe the effect of inter-particle bonding on the irreversible volumetric behavior of the soil, based on the experimental observation that e/e_s increases with increasing values of the bonding factor ζ :

$$\frac{e}{e_s} = h(\zeta) = 1 + a \zeta^b \quad (16)$$

where a and b are fitting parameters while e and e_s are the void ratios corresponding to the unsaturated and saturated states at the same value of average skeleton stress. Note that e_s is related to the average skeleton stress (which coincides with Terzaghi's effective stress in the saturated case) by the saturated normal compression line:

$$e_s = e_s(p') = N - \lambda \ln p' \quad (17)$$

where N is the void ratio corresponding to $p' = 1 \text{ kPa}$, and λ is the slope of the saturated normal compression line in the $\ln p' - e_s$ plane.

3.3. Experimental evidence

Experimental data from laboratory tests (corresponding to isotropic and triaxial stress states) are here used to validate Eq. (16). For each experimental data set [41–45], the parameters N and λ in Eq. (17) have been calibrated from saturated isotropic loading tests (Table 1). During unsaturated loading, the void ratio e , the mean net stress p_{net} , the degree of saturation S_r and the suction s were also recorded (note that the degree of saturation depends on both suction and void ratio). The bonding factor $\zeta = (1 - S_r^{1/4})/g(e)$, the saturated void ratio $e_s = N - \lambda \ln(p_{\text{net}} + S_r \cdot s)$, and the ratio e/e_s could therefore be calculated. The measured values of ζ and e/e_s were then fitted by Eq. (16) using the least-square method and the parameters a and b were finally obtained as shown in Table 1. The above procedure was also employed to validate Eq. (16) at critical states but, in this case, the saturated critical state line was used instead of the saturated normal compression line.

Fig. 4 shows the fitting of Eq. (16) to different soil data corresponding to both isotropic and critical states. The soils are reconstituted kaolin (Fig. 4a) [42], bentonite/kaolin mixture (Fig. 4b) [43], speswhite kaolin (Fig. 4c) [45], Barcelona clayey silt (Fig. 4d) [44], Kiunyu gravel ($19.6\% \leq w \leq 21.9\%$) (Fig. 4e) [41], Kiunyu gravel at critical state ($24.9\% \leq w \leq 27.7\%$) (Fig. 4f) [41] and reconstituted kaolin (Fig. 4g) [42]. A remarkable correlation exists between e/e_s and ζ under isotropic loading (Fig. 4a–d), at critical state (Fig. 4e–g) and during wetting (Fig. 4d), with values of the correlation coefficient (R^2) above 0.93. Fig. 4g also suggests the existence

Table 1
Calibration of Eq. (16) for different soils and different stress states.

Soil names	Stress state	Parameters				R^2
		N	λ	a	b	
Reconstituted kaolin [42]	Normal compression state	1.046	0.112	21.096	1.208	0.975
Bentonite/kaolin mixture [43]		1.759	0.144	13.872	1.059	0.992
Speswhite kaolin [45]		1.530	0.130	6.143	0.812	0.987
Barcelona clayey silt [44]		0.934	0.072	5.655	1.085	0.971
Kiunyu gravel [41]	Critical state	1.430	0.094	1.580×10^3	2.888	0.933
Kiunyu gravel [41]		1.430	0.094	7.753×10^2	2.325	0.960
Reconstituted kaolin [42]		1.518	0.110	21.096	1.208	0.981

of a unified relationship between e/e_s and ζ under both isotropic and triaxial stress states.

Inspection of Fig. 4 indicates that the ratio e/e_s decreases with decreasing bonding factor ζ consistent with Eq. (16). Physically, this is explained by the fact that a decreasing value of the bonding factor (or bonding force) can induce a relatively large slippage between soil particles, and therefore reduces pore space.

4. Constitutive model

This section presents a constitutive model, for both isotropic and triaxial stress states, based on the consideration of the bonding factor of Eq. (16), while Section 5 focuses on the validation of the model against experimental observations.

4.1. Constitutive model for isotropic stress states

Plastic deformation of an unsaturated soil is caused by changes of both average skeleton stress and capillary bonding. Thus, the void ratio under unsaturated conditions is calculated as

$$e = \frac{e}{e_s} \cdot e_s = h(\zeta)e_s \quad (18)$$

where $h(\zeta)$ (Eq. (16)) represents the effect of the bonding force exerted by inter-particle water menisci under unsaturated conditions. Similar treatment was presented by Gallipoli et al. [25], though our formulation of the bonding factor is different from theirs.

The elastic change in void ratio (de^e) is expressed as a function of the change of mean average skeleton stress (dp'),

$$de^e = -\kappa \frac{dp'}{p'} \quad (19)$$

where κ is the slope of the elastic swelling line in the e - $\ln p'$ plane and is assumed to be the same under saturated and unsaturated conditions. Here, we neglect elastic strains induced by changes of the bonding factor (i.e. changes of saturation) under constant average skeleton stress. This assumption is best suited to describe the behavior of silt or low plasticity clays. For highly expansive soils, however, the development of elastic strains due to changes of the bonding factor (or saturation) requires further examination.

Fig. 5 shows a three-dimensional view of the normal compression surface defined by Eq. (18) in the $\ln p' - e - \zeta$ space. Consider an elastic drying path under constant average skeleton stress from A to B' followed by an elastic loading path from B' to B at constant bonding factor. The plane identified by the paths A \rightarrow B' and B' \rightarrow B is an elastic wall where only reversible volumetric strains can occur. On the other hand, irreversible volumetric strains occur when the soil state moves on the normal compression surface. Thus, the intersection of the elastic wall with the three-dimensional normal compression surface of Fig. 5 defines the current yield curve. Given that no elastic strains are generated by a variation of the bonding factor, the elastic change of void ratio between points B and A (both belonging to the normal compression surface) is entirely due to the change of mean average skeleton stress from B' to B:

$$e - (N - \lambda \ln p'_c(0)) = -\kappa(\ln p' - \ln p'_c(0)) \quad (20)$$

The expression of the normal compression surface of Fig. 5 is calculated from Eqs. (17) and (18) as

$$e = h(\zeta)(N - \lambda \ln p') \quad (21)$$

The expression of the yield curve f , given by the intersection of the elastic wall with the normal compression surface, is finally obtained by combining Eqs. (20) and (21):

$$f(p', \zeta, p'_c(0)) = (h(\zeta)\lambda - \kappa) \ln p' - (\lambda - \kappa) \ln p'_c(0) - N(h(\zeta) - 1) = 0 \quad (22)$$

where $p'_c(0)$ is the mean yield average skeleton stress under saturated conditions. The yield curve of Eq. (22) provides a good fit to the initial yield stresses measured during loading at constant suction in two different experimental campaigns [43,46] (Fig. 6).

During a plastic stress path, the irreversible change of void ratio is obtained by subtracting the elastic change from the total change,

$$\Delta e^p = \Delta e - \Delta e^e = [e_s(p'_2)h(\zeta_2) - e_s(p'_1)h(\zeta_1)] - \Delta e^e \quad (23)$$

where p'_1 , ζ_1 and p'_2 , ζ_2 are the average skeleton stress and bonding factors corresponding to the starting and end points of a stress path, respectively. The superscripts e and p refer to elastic and plastic components, respectively.

4.2. Constitutive model for triaxial stress states

This section extends the above constitutive model from isotropic stress states to triaxial stress states by adopting a framework similar to that of the Modified Cam-clay model [47].

4.2.1. Yield function

Following Alonso et al. [11], the extension to triaxial stress states is achieved by combining the above model for isotropic stress states with the yield surface of Modified Cam-clay [47]:

$$f = q^2 - M^2 p' [p'_c(\zeta, p'_c(0)) - p'] = 0 \quad (24)$$

where q is the deviator stress, M is the slope of the critical state line in the q - $\ln p'$ plane and $p'_c(\zeta, p'_c(0))$ is the yield value of the average skeleton stress at a specific value of ζ defined by Eq. (22) as:

$$p'_c(\zeta, p'_c(0)) = \exp \left\{ \frac{(\lambda - \kappa) \ln p'_c(0) + N(h(\zeta) - 1)}{h(\zeta)\lambda - \kappa} \right\} \quad (25)$$

Fig. 7 shows that the intersections of the triaxial yield surface with the p' - ζ plane and the p' - q plane coincide with the isotropic yield curve and the Modified Cam-clay yield ellipse, respectively.

4.2.2. Flow rule

A non-associated flow rule is chosen

$$g = \eta q^2 - M^2 p' [p'_c(\zeta, p'_c(0)) - p'] = 0 \quad (26)$$

where η is a constant determined by imposing zero lateral strains under K_0 conditions [11], which results in $\eta = [M(M - 9)(M - 3)\lambda] / [9(6 - M)(\lambda - \kappa)]$ [48].

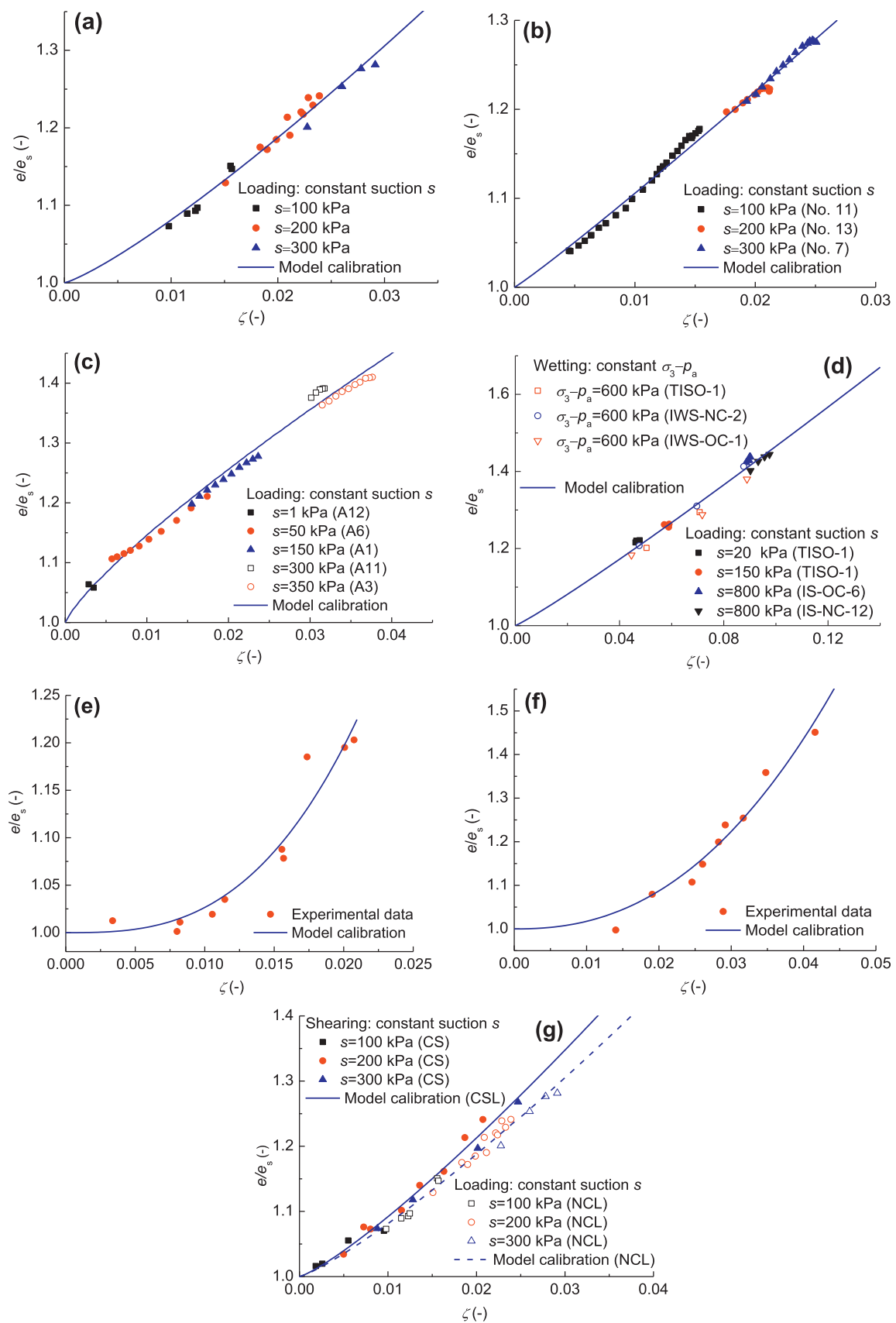


Fig. 4. Fitting of Eq. (16) to experimental data for different soils and different stress states: (a)–(d) isotropic normal compression, (a) reconstituted kaolin, data from Sivakumar [42], (b) bentonite/kaolin mixture, data from Sharma [43], (c) speswhite kaolin, data from Raveendiraraj [45], (d) Barcelona clayey silt, data from Barrera [44] (note that in [44], the labels “NC” and “OC” indicate normal consolidated and overconsolidated soil samples, respectively, and the initial void ratio and water content of the wetting tests are different); (e)–(g) at critical state, (e) Kiunyu gravel ($19.6\% \leq w \leq 21.9\%$), data from Toll [41], (f) Kiunyu gravel at critical state ($24.9\% \leq w \leq 27.7\%$), data from Toll [41], (g) reconstituted kaolin data from Sivakumar [42].

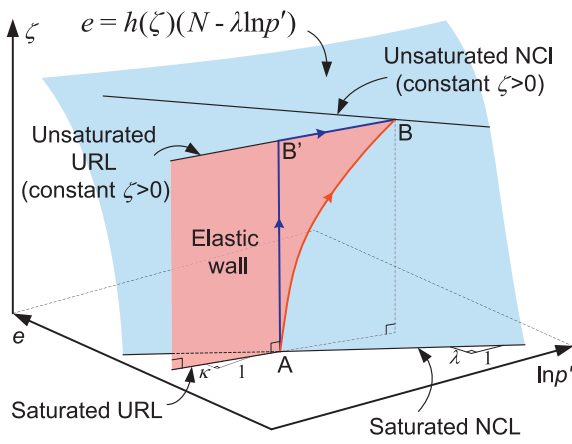


Fig. 5. Normal compression state surface and yield curve. NCL: normal compression line, URL: unloading reloading line. Note that the saturated/unsaturated NCL lines are on the compression state surface.

The incremental plastic volumetric and shear strains can be obtained from

$$de_v^p = A \frac{\partial g}{\partial p'} \quad (27)$$

$$de_s^p = A \frac{\partial g}{\partial q} \quad (28)$$

where A is the plastic multiplier determined from the consistency condition

$$df = \frac{\partial f}{\partial q} dq + \frac{\partial f}{\partial p'} dp' + \frac{\partial f}{\partial zeta} dzeta + \frac{\partial f}{\partial e_v^p} de_v^p = 0 \quad (29)$$

where

$$\left. \begin{aligned} \frac{\partial f}{\partial q} &= 2q \\ \frac{\partial f}{\partial p'} &= M^2(2p' - p'_c(zeta)) \\ \frac{\partial f}{\partial zeta} &= \frac{\partial f}{\partial p'_c(zeta)} \frac{\partial p'_c(zeta)}{\partial zeta} \\ \frac{\partial f}{\partial e_v^p} &= \frac{\partial f}{\partial p'_c(zeta)} \frac{\partial p'_c(zeta)}{\partial p'_c(0)} \frac{\partial p'_c(0)}{\partial e_v^p} \\ \frac{\partial f}{\partial p'_c(zeta)} &= -M^2 p' \\ \frac{\partial p'_c(zeta)}{\partial zeta} &= \frac{(N - \lambda \ln p'_c(zeta))}{h(zeta)\lambda - \kappa} \frac{\partial h(zeta)}{\partial zeta} p'_c(zeta) \\ \frac{\partial p'_c(zeta)}{\partial p'_c(0)} &= \frac{p'_c(zeta)}{p'_c(0)} \frac{\lambda - \kappa}{h(zeta)\lambda - \kappa} \\ \frac{\partial p'_c(0)}{\partial e_v^p} &= \frac{1+e}{\lambda - \kappa} p'_c(0) \\ \frac{\partial h(zeta)}{\partial zeta} &= abzeta^{b-1} \end{aligned} \right\} \quad (30)$$

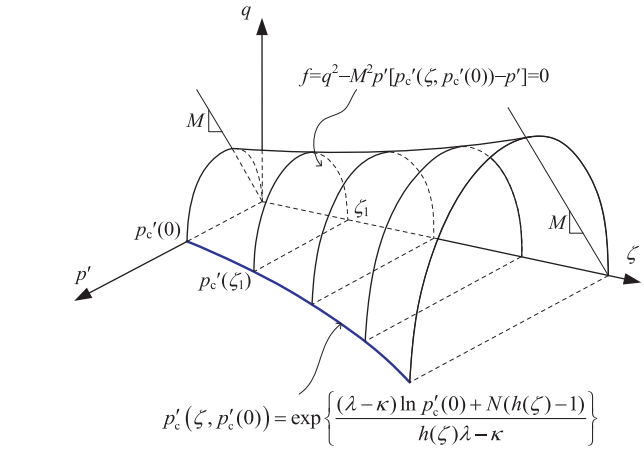
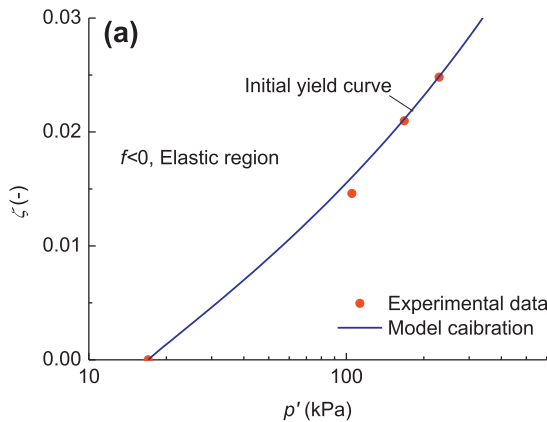


Fig. 7. Three-dimensional view of yield surface.

From Eqs. (24)–(30), the incremental plastic volumetric and shear strains can be derived as

$$de_v^p = \frac{h(zeta)\lambda - \kappa}{1+e} \frac{2q dq}{M^2 p'^2 + q^2} + \frac{h(zeta)\lambda - \kappa}{1+e} \frac{M^2 p'^2 - q^2}{M^2 p'^2 + q^2} \frac{dp'}{p'} - \frac{(N - \lambda \ln p'_c(zeta))}{1+e} \frac{\partial h(zeta)}{\partial zeta} dzeta \quad (31)$$

$$de_s^p = \frac{2\eta p' q}{M^2 p'^2 - q^2} de_v^p \quad (32)$$

The elastic volumetric and shear strain, on the other hand, can be generally expressed by

$$de_v^e = \frac{\kappa}{1+e} \frac{dp'}{p'} = \frac{dp'}{K} \quad (33)$$

$$de_s^e = \frac{dq}{3G} \quad (34)$$

where $K = (1+e)p'/\kappa$ and $G = 2K(1-2\mu)/[3 \times (1+\mu)]$ are the elastic bulk and shear modulus, respectively, and μ is Poisson's ratio.

4.2.3. Hardening rule

The saturated yield average skeleton stress, $p'_c(0)$, which depends on the accumulated plastic volumetric strain, controls the evolution of the yield surface during plastic loading and is therefore chosen as the hardening parameter. The hardening rule of the yield surface is expressed as:

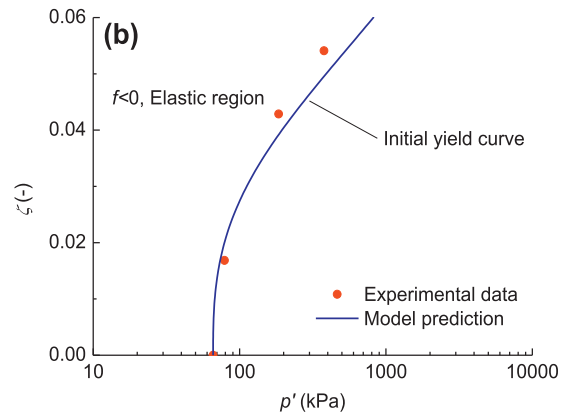


Fig. 6. Comparisons between calculated and observed yield curves during loading at constant suctions: (a) bentonite/kaolin mixture, data from Sharma [43]; (b) Jossigny silt, data from Gallipoli et al. [46].

$$\frac{dp'_c(0)}{p'_c(0)} = \frac{1+e}{\lambda-\kappa} de_v^p \quad (35)$$

where de_v^p is the incremental plastic volumetric strain determined by Eq. (31).

4.3. Model parameters

The proposed model has eight parameters: N , λ , κ , $p'_c(0)$, a , b , M , and G . Four parameters (N , λ , κ , and $p'_c(0)$) can be easily determined from saturated isotropic compression tests. Since e/e_s increases with ζ , the parameters a and b must be both positive, and their values can be determined from suction-controlled compression tests. Drained shear tests at constant suction can be used to determine the values of M and G (or M and μ).

If the soil is over-consolidated (i.e. the soil stress state lies on an elastic swelling line), the initial void ratio e_i is calculated from Eq. (19) as:

$$e_i = e_0 - \kappa \ln \frac{p'_i}{p'_c(0)} \quad (36)$$

where $e_0 = N - \lambda \ln p'_c(0)$ is the void ratio corresponding to the initial value of the hardening parameter, $p'_c(0)$, and p'_i is the initial value of the mean average skeleton stress.

Note that the degree of saturation appears in the definition of the constitutive variables and, therefore, knowledge of the water retention curve is required to make the model closed. In the present study, however, experimental rather than calculated values of degree of saturation have been used in the simulations due to the fact that the proposed model only describes mechanical behavior. When the hysteretic water retention curve model [49,50] was incorporated into the proposed model to predict the coupled hydro-mechanical behavior of unsaturated soils, the results were not as accurate. Further work should be conducted to investigate incorporation of the SWRC into the model.

4.4. Model discussion

Eqs. (16) and (17) show that the variation of e with mean average skeleton stress p' can be written as:

$$e = N(\zeta) - \lambda(\zeta) \ln p' \quad (37)$$

where $N(\zeta) = N(1 + a\zeta^b)$, and $\lambda(\zeta) = \lambda(1 + a\zeta^b)$.

In Eq. (37), the parameters N and λ are both functions of the bonding factor, which indicates that the volumetric compressibility of the soil depends on the bonding factor. This is different from the model of Alonso et al. [11], where the volumetric compressibility of the soil is assumed to depend solely on suction. Recently, in the constitutive model by Zhou et al. [24], the volumetric compressibility has been related solely to the effective degree of saturation, and the parameter N is assumed to be a constant.

As shown in Eq. (37), the soil compressibility $\lambda(\zeta) = \lambda(1 + a\zeta^b)$ is a power function of the bonding factor and therefore depends on both degree of saturation and void ratio. The parameters a and b should correlate with basic soil properties, including plasticity index, effective grain size, etc., though further research on this issue is required. Because of the particular definition of the bonding factor (Eq. (14)), the void ratio appears on both sides of Eq. (37). In order to simplify the numerical implementation of the proposed model, the simulations presented in this paper assume that the void ratio on the right-hand side of Eq. (37) is known and equal to the value calculated in the previous substep of the simulation. This is acceptable as long as the size of each substep is small enough.

5. Model validation

In this section, predictions from the proposed model are compared with experimental data [43,51,46,45], to demonstrate the effectiveness of the model in describing the mechanical behavior of unsaturated soils, including the prediction of (a) the initial yield surface measured during suction-controlled oedometer and isotropic compression tests, (b) the irreversible/reversible changes of void ratio induced by wetting–drying cycles and (c) the influence of wetting–drying cycles on subsequent isotropic loading/shearing. In the following figures, we use the expression “model results” if the data shown in the figure has been already used for the model calibration. Otherwise, we use the expression “model predictions”. Although the relationship of Eq. (16) was not validated during drying paths, the results presented in the following sections suggest that the same relationship between e/e_s and ζ can also be used for the simulation of drying paths.

5.1. Oedometer tests from MUSE Benchmark B9 [46]

In the MUSE Benchmark B9, constant suction oedometer tests on compacted samples of Jossigny silt were presented. Model parameters λ , N , κ , and $p'_c(0)$ were calibrated from the saturated test EDO-sat while the values of a and b were determined from oedometer tests at constant suctions of 100 kPa (EDO-100) and 200 kPa (EDO-200). Therefore, according to the terminology previously introduced, the simulations of EDO-100 in Fig. 8e are “model results” whereas the simulations of tests EDO-10 and EDO-50 in Fig. 8a and c are “model predictions”. The values of model parameters are listed in Table 2. The initial void ratios of the different tests were predicted from Eq. (36), with e_i being 0.819, 0.816 and 0.814 for constant suctions of 10 kPa, 50 kPa and 100 kPa, respectively. The inaccurate prediction by Eq. (36) of the initial void ratio for the test EDO-100 (with an error of about 7%, see Fig. 8e) might be due to limitations of the adopted elastic law. One way of improving the prediction of the initial void ratio, without changing the elastic law, would be to choose a greater initial value of the hardening parameter, $p'_c(0)$. However, given that the initial value of the hardening parameter also fixes the position of the initial yield curve (Fig. 6b), this will have the undesirable consequence of deteriorating the prediction of the yield stresses.

Samples EDO-10, EDO-50 and EDO-100 were loaded from a vertical net stress $\sigma_v - u_a = 20$ to 800 kPa, followed by unloading from 800 to 100 kPa and then reloading to 1200, 1226, and 1080 kPa, respectively.

Before point A, the response was elastic (Fig. 8a, c and e). Then the initial yield curve C0 was attained and substantial irreversible changes in void ratio occurred, producing an expansion of the yield curve from C0 to C1 (corresponding to point B). The initial yield surface calculated from Eq. (22) agrees well with the observed yield stress (see also Fig. 6b). Soil deformation was elastic during the unloading–reloading stage (BCC'). During plastic loading from C' to D, the samples experienced hardening of the yield surface to the final position C2. All the experimental data are reasonably well represented by the proposed model.

Fig. 8b, d and e show abrupt changes in stress path (p' – ζ) at several points (denoted by Pt₁). In order to explain this behavior, the variation of degree of saturation was also plotted. In Fig. 8b, the slope of the stress path at point Pt₁ changes suddenly due to the corresponding abrupt change in degree of saturation. In the cases of constant suctions of 50 kPa and 100 kPa, these abrupt changes of stress path correspond to local maxima in the p' – ζ plane. This is because, before the maxima point (Pt₁), the void ratio decreases while the degree of saturation increases. The decrease of e results in an increase of ζ while the increase of S_r results in a decrease of

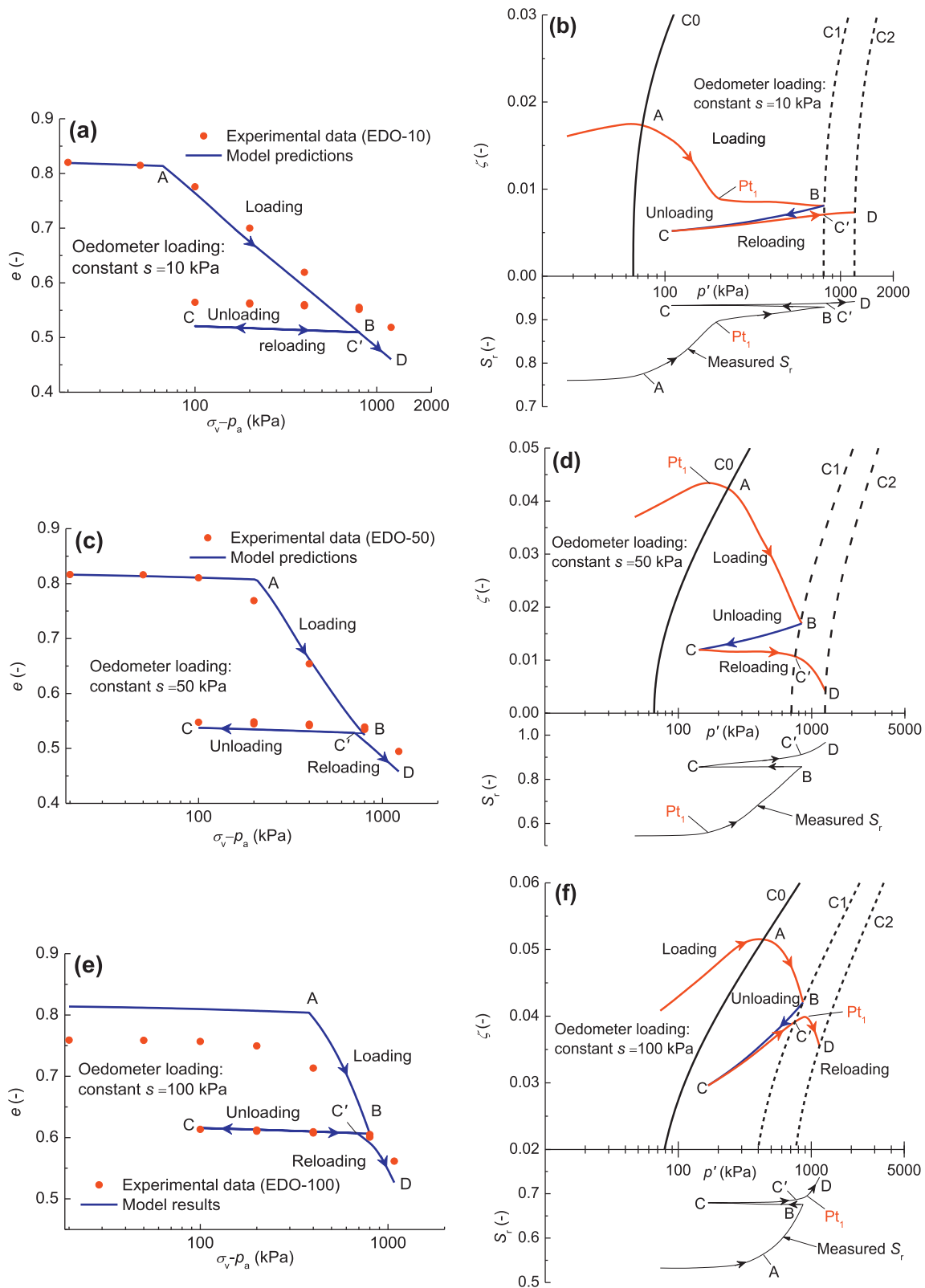


Fig. 8. Comparison between model predictions/results and experimental data during oedometer loading (data from [46]): (a) and (b) at constant suction of 10 kPa, EDO-10; (c) and (d) at constant suction of 50 kPa, EDO-50; (e) and (f) at constant suction of 100 kPa, EDO-100; (left side) (a, c, e): void ratio–mean net stress; (right side) (b, d, f): stress path and variation of degree of saturation.

ζ , with the former effect being the dominant one. Then, at point Pt_1 (with $p' = 166.1$ kPa for constant $s = 50$ kPa and with $p' = 890.0$ kPa for constant $s = 100$ kPa), the effect of increasing S_r becomes dom-

inant and ζ reaches a local maxima in the $p' - \zeta$ plane. Note that in Fig. 8d, the point Pt_1 is just inside the elastic zone whereas the point Pt_1 in Fig. 8b and f is on the yield surface.

Table 2

Soil parameters for Jossigny silt (MUSE Benchmark B9) [46].

Parameter	Value
λ	0.122
N	1.325
κ	5.628×10^{-3}
a	1.604×10^3
b	2.818
$p'_c(0)$	65.93 kPa

Fig. 8 also indicates that the stress path during elastic unloading BC does not coincide with the stress path during the subsequent elastic reloading CC', though the corresponding curves overlap perfectly in the $e-p_{\text{net}}$ plane. This is again a consequence of the slight different variation of degree of saturation during elastic unloading and subsequent elastic reloading.

5.2. Experiments by Sharma [43]

Laboratory tests by Sharma [43] demonstrated several important features of the mechanical behavior of a compacted mixture of bentonite/kaolin, including yielding at constant suction during isotropic loading, irreversible change of void ratio induced by wetting/drying, and the influence of wetting–drying cycles on subsequent isotropic loading. The tests involved a combination of isotropic loading at constant suction and wetting–drying at constant mean net stress. The model parameter values derived from these tests are listed in Table 3. The κ value is taken from Sharma [43], while the values of N , λ , and $p'_c(0)$ are the same as those reported in Gallipoli et al. [25]. The suction-controlled tests No. 7 ($s = 300$ kPa), No. 11 ($s = 100$ kPa) and No. 13 ($s = 200$ kPa) were used to determine the values of a and b . Since the data of Test No. 7 and No. 11 were also used for comparison purposes, the computed curves in Fig. 9a and e represent “model results” while all other curves are “model predictions”. The initial void ratio was predicted by Eq. (36) based on the initial value of the hardening parameter $p'_c(0)$.

5.2.1. Isotropic loading at constant suction

Fig. 9 presents comparisons between model simulations and experimental data. The corresponding stress paths and yield surfaces are also shown. The initial yield curves were attained at point A corresponding to mean average skeleton stress values of 105, 168, and 229 kPa for suctions of 100, 200 and 300 kPa, respectively. These yield stresses are well predicted by the simulated yield curve (Fig. 6a). After point A, irreversible changes of void ratio occurred, and the yield curve expanded from C0 to C1 at the end of loading (point B). During the unloading path (BC), all samples experienced elastic deformation. For the test at a constant suction of 200 kPa, the yield curve was further expanded from C1 to C2 during the second loading. In general, model simulations agree well with experimental data.

Table 3

Soil parameter values for bentonite/kaolin [43].

Parameter	Value
λ	0.144
N	1.759
κ	0.040
a	13.872
b	1.059
$p'_c(0)$	17.0 kPa

5.2.2. Wetting–drying cycles at constant net stresses

Fig. 10a shows a comparison between predicted and observed behavior during a wetting–drying cycle at a constant mean net stress of 50 kPa. During wetting, suction decreased and S_r increased, causing a reduction of the average skeleton stress (Fig. 10b). Before point A, the stress path lay within the initial yield surface, and the behavior is elastic. Plastic collapse happens during the wetting stage AC. However, the wetting-induced irreversible change in void ratio during path AB is much smaller than during the path BC. This is because the stress path AB intersects the current yield curve at a gentler angle than path BC. It is worth mentioning that, during path BC, the mean net stress and suction were kept unchanged, and a marked increase of degree of saturation (likely to be due to lack of equalization during path AB) induced considerable irreversible compression, which is reasonably captured by the model. When suction reversed (CD), irreversible changes in void ratio occurred over the entire drying path, even if suction did not exceed the maximum value previously applied. This is an important feature of the mechanical behavior of unsaturated soils [17] that is often not captured by previous models.

As reported by Sharma [43] and Gallipoli et al. [25], the incomplete equalization of suction during the wetting–drying cycle may be an explanation for the discrepancy between experimental data and model predictions.

Fig. 10c shows a comparison between experimental data and predicted soil behavior during wetting–drying cycles at a constant mean net stress of 20 kPa. Unlike Fig. 10a, only elastic swelling took place here during the first and second wetting, while irreversible changes of void ratio occurred during the drying stage AB, bringing the yield curve from C0 to C1.

Fig. 10e shows model predictions and experimental data during wetting–drying cycles at a constant mean net stress of 10 kPa. The sample response was elastic during the two wetting stages, whereas irreversible changes of void ratio occurred during the first and second drying stages (AB and DE) (Fig. 10f). The first drying stage AB resulted in the hardening of the yield curve from C0 to C1. The stress path remained inside the elastic domain throughout the second wetting, with no expansion of yield curve, and the sample approached nearly saturated conditions ($S_r = 0.94$) at the end of the second wetting stage (C'). Finally, the second drying path expanded the yield locus from C1 to C2.

Fig. 10b, d and f show the variation of the bonding factor and degree of saturation with average skeleton stress. The abrupt changes in direction of the stress path at points Pt₁, Pt₂, and Pt₃ are due to the corresponding sudden changes in the slope of the saturation curve, which is induced by the lack of equalization during the experiment.

A large elastic swelling was observed during wetting stage of CC' (Fig. 10f), where the bonding factor decreased rapidly while net stress and suction remained unchanged. Unlike the stage BC in Fig. 10a that the sample underwent irreversible compression volumetric deformation under relatively high stress condition (50 kPa), at the stage C'C in Fig. 10e, an increase of degree of saturation with a low stress condition (10 kPa) can cause the reversible swelling volumetric deformation, and it cannot be reproduced by the proposed model, indicating that the relationship (Eq. (19)) is not adequate for the expansive soil. The inadequate relationship for swelling volumetric deformation may also induce a discrepancy between model results and experimental data in the drying path AB (Fig. 10e). As shown in Fig. 10e, a concave upward trend was predicted, while the experimental data shows a concave downward trend. Nevertheless, the predicted results capture the main features of experimental data.

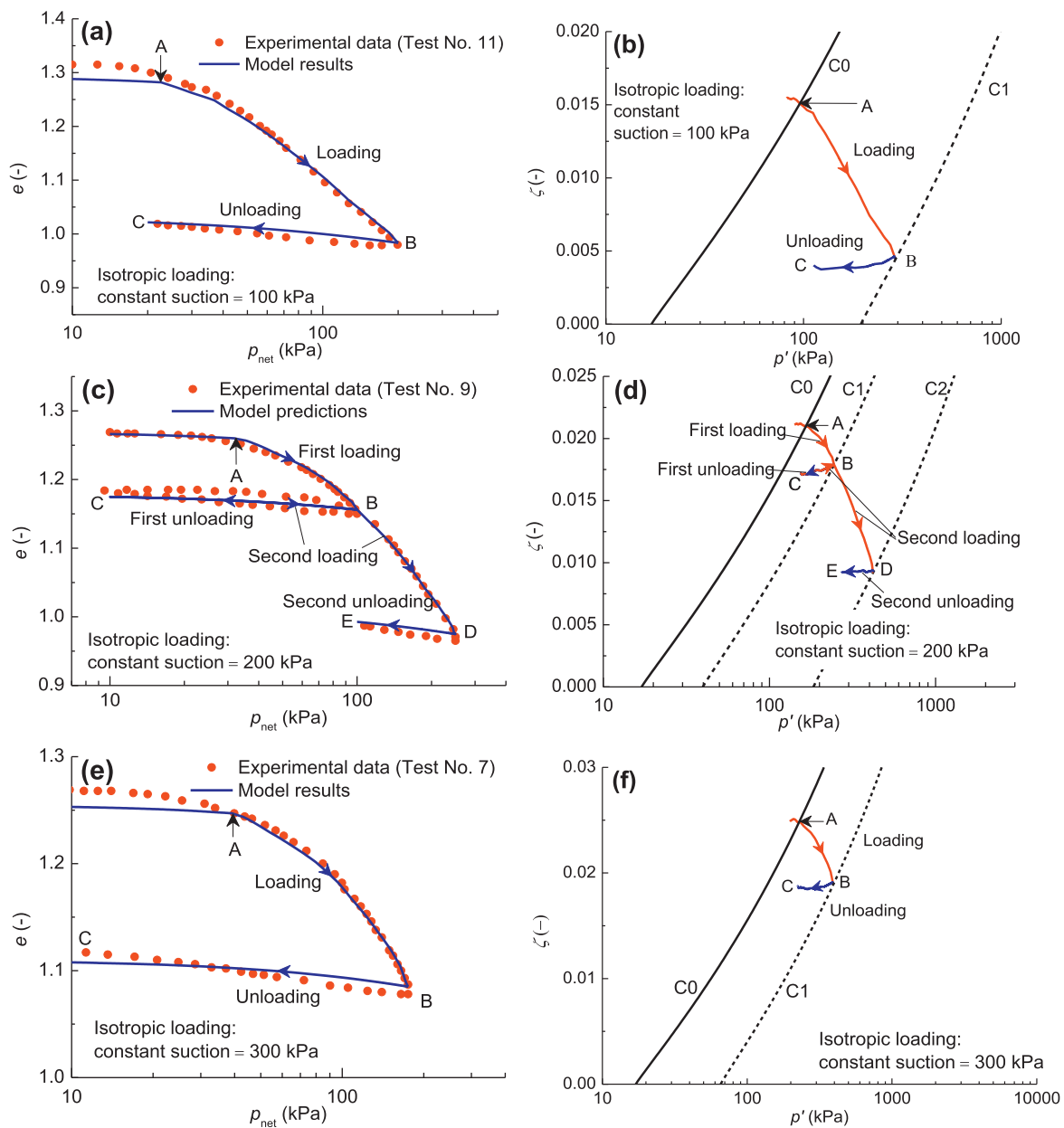


Fig. 9. Comparison between model predictions/results and experimental data during isotropic loading (data from [43]): (a) and (b) at constant suction of 100 kPa, Test No. 11; (c) and (d) at constant suction of 200 kPa, Test No. 9; (e) and (f) at constant suction of 300 kPa, Test No. 7; (left side) (a, c, e): void ratio–mean net stress; (right side) (b, d, f): stress path.

5.2.3. Influence of wetting–drying cycles on subsequent isotropic loading

Fig. 11 compares observed and predicted behavior during isotropic loading of two samples at a constant suction of 300 kPa. One sample was subjected to a wetting–drying cycle prior to loading (suction: 300 kPa → 20 kPa and 20 kPa → 300 kPa) while the other one did not. As shown in Fig. 11c, in the case of the former sample, the stress state lays after the wetting–drying cycle on the yield curve and irreversible change therefore occurred immediately during subsequent loading. Instead, in the case of the sample that was not subjected to the wetting–drying cycle, loading started from inside the yield curve and yielding was only attained after loading progressed. The simulated deformations are generally in agreement with observations, indicating that the proposed model is able to capture the history of suction variation. Note that the abrupt change in the slope of the stress path at point Pt₁

(Fig. 11c) corresponds to a change in the trend of variation of degree of saturation, which is again due to lack of equalization during the experiment.

5.3. Experiment by Sivakumar [51]

Experimental data from Sivakumar [51] were used to evaluate the proposed model under a variety of triaxial stress paths. The tests were conducted on compacted kaolin under constant suction. The samples had a clay content of about 80%, with liquid and plastic limits of 70% and 36%, respectively. The values of the model parameters for this soil are listed in Table 4. In particular, the values of parameters λ , N , κ , $p_c(0)$ and μ were determined from saturated test data while the values of parameters a and b were determined from isotropic compression tests at constant suctions of 100, 200 and 300 kPa.

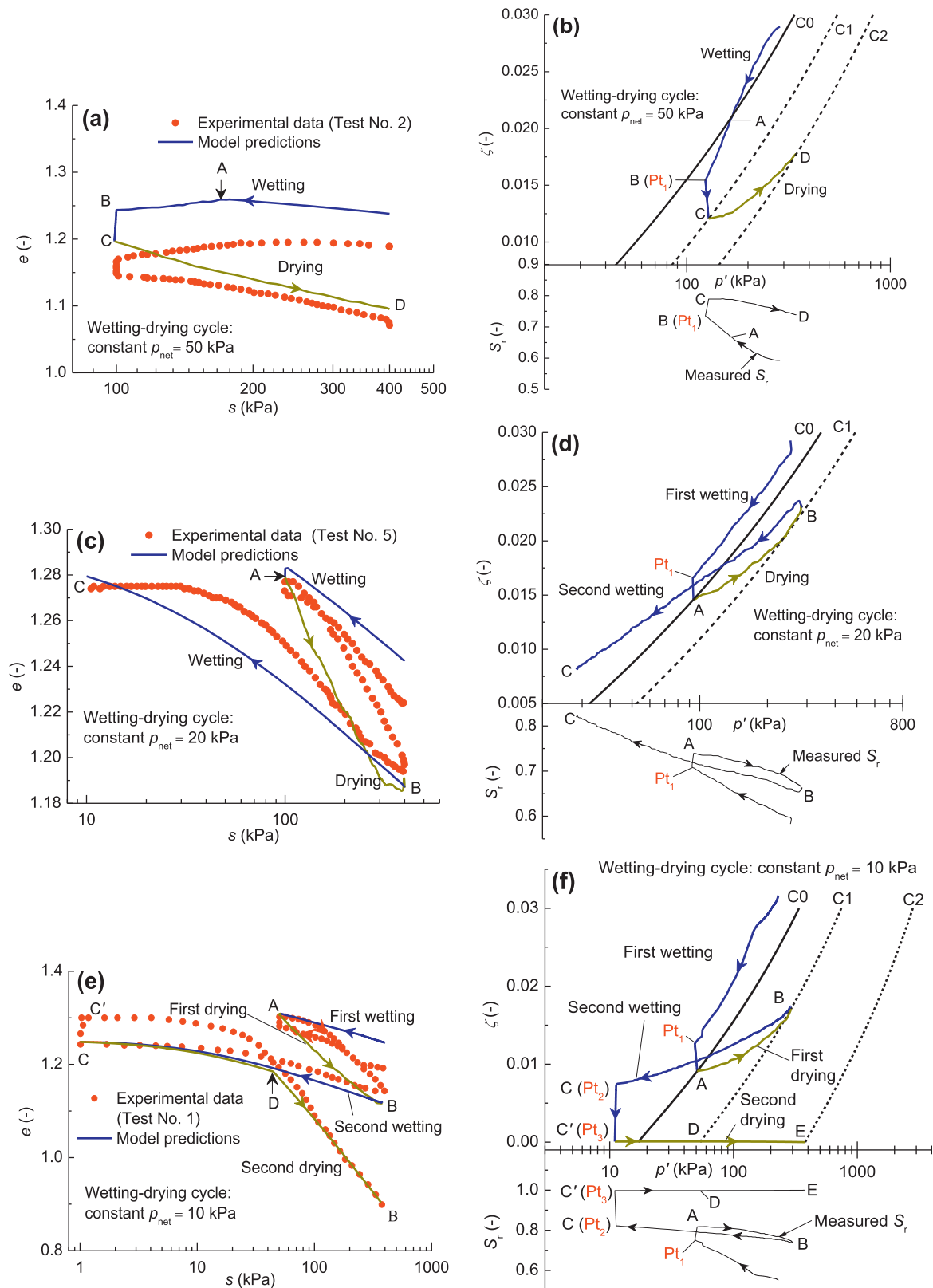


Fig. 10. Comparison between model predictions and experimental data for wetting–drying cycle (data from [43]): (a) and (b) at constant net stress of 50 kPa, Test No. 2; (c) and (d) at constant net stress of 20 kPa, Test No. 5; (e) and (f) at constant net stress of 10 kPa, Test No. 1; (left side) (a, c, e) void ratio–suction; (right side) (b, d, f) stress path and variation of degree of saturation.

Samples were first isotropically compressed and subsequently sheared to critical state. The void ratios at the start of shearing were predicted by Eq. (36) based on the initial value of the harden-

ing parameter $p'_c(0)$. The simulated stress paths can be categorized into three groups: (1) constant mean net stress ($p_{\text{net}} = 200$ kPa), (2) constant radial net stress ($\Delta q/\Delta p_{\text{net}} = 3$), and (3) curved stress path.

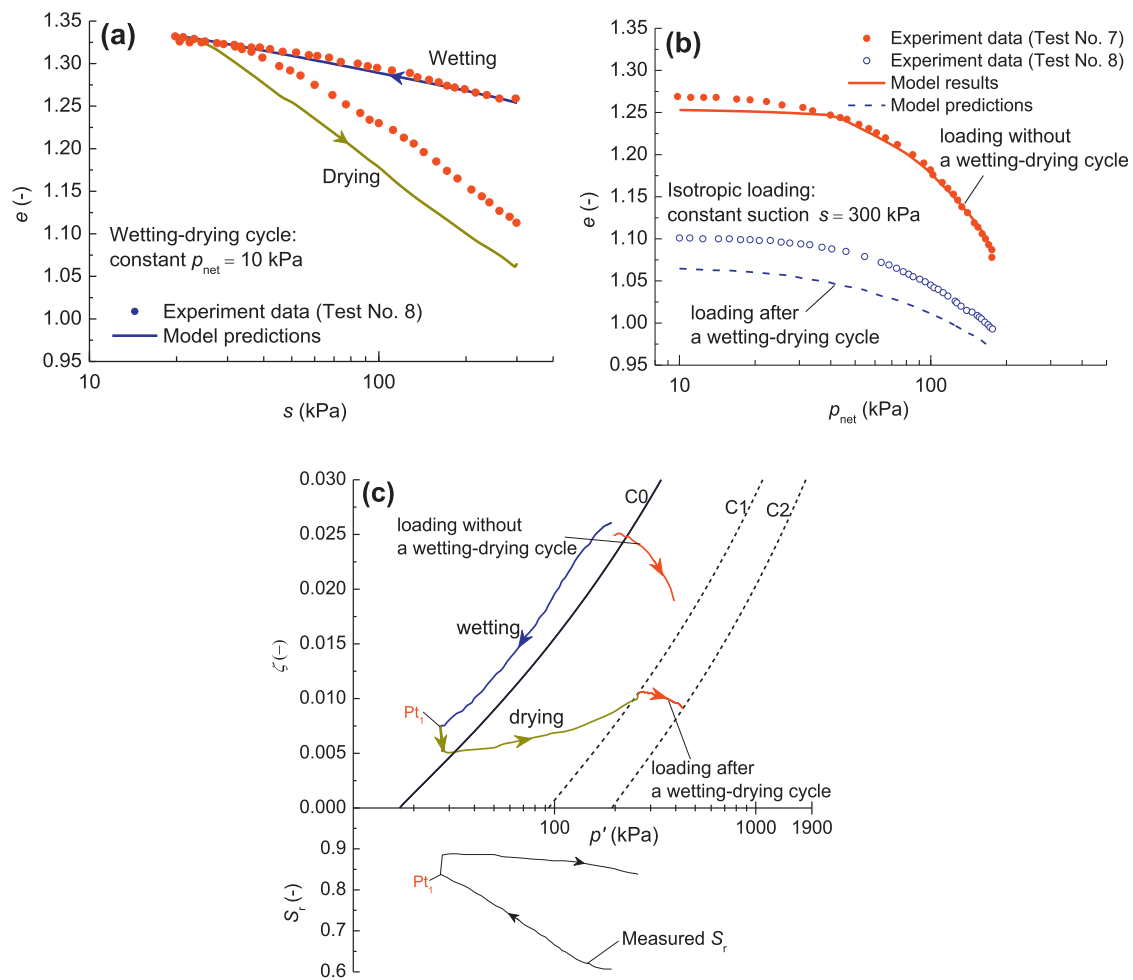


Fig. 11. Comparison between model predictions/results and experimental data for isotropic loading (with/without previous wetting–drying cycle at constant mean net stress of 10 kPa) (data from [43]): (a) change of void ratio during wetting–drying cycle; (b) change of void ratio during loading; (c) stress paths and variation of degree of saturation.

In order to quantify the curved stress path, a mathematical function $(p_{net}/a_1)^2 + (q/b_1)^2 = 1$, with $a_1 = 200$ kPa, $b_1 = 279$ kPa, was fitted to the test stress path of Sivakumar [51]. The tests in the first group were conducted at constant suctions of 100 and 200 kPa; the tests in the second group at suctions of 100, 200, and 300 kPa; the tests in the third group were conducted at a suction of 200 kPa only.

Fig. 12 shows comparisons between experimental data and model predictions in terms of axial strains, volumetric strains, and void ratio for the three different test groups. Consistent with the theories of critical state soil mechanics, observed axial strains increased monotonically whereas the deviator stress q and the volumetric strain ϵ_v increased initially and then reached nearly the ultimate values at the end of shearing. The observed shearing

behavior is reasonably reproduced by the proposed model. At the end of the simulation, the observed and predicted values of deviator stress (listed in Table 5) show that the maximum prediction error is 7.8%. The changes in void ratio are plotted in Fig. 12b, d and f, indicating good agreement between predicted and observed results.

With the exception of the shearing test under constant radial net stress at a suction of 300 kPa, all other tests in Fig. 12 involve stress paths that remain on the yield surface during the whole shearing processes. In the case of the test under constant radial net stress at a suction of 300 kPa (Fig. 12g), the mechanical response is elastic before point A and elasto-plastic after point A. Fig. 12 also shows that, during the initial stages of shearing, the model tends to slightly under-predict shear strains, mostly due to the particular choice of non-associative flow rule.

Table 4

Soil parameter values for shearing tests on kaolin [51].

Parameter	Value
M	0.858
N	1.835
λ	0.142
κ	0.034
a	11.080
b	1.066
$p'_c(0)$	63.0 kPa
μ	0.35

5.4. Experiments by Raveendiraraj [45]

Experimental data for speswhite kaolin published by Raveendiraraj [45] were used to further verify the proposed model for different stress paths, including isotropic loading, wetting–drying cycles, shearing, and combinations thereof. The values of model parameters λ , N , κ , $p'_c(0)$ were determined from saturated tests [45], and the value of G was calibrated from shearing tests at constant radial net stress of 75 kPa and suctions of 200 and 300 kPa. Parameters a and b were calibrated from the suction-controlled

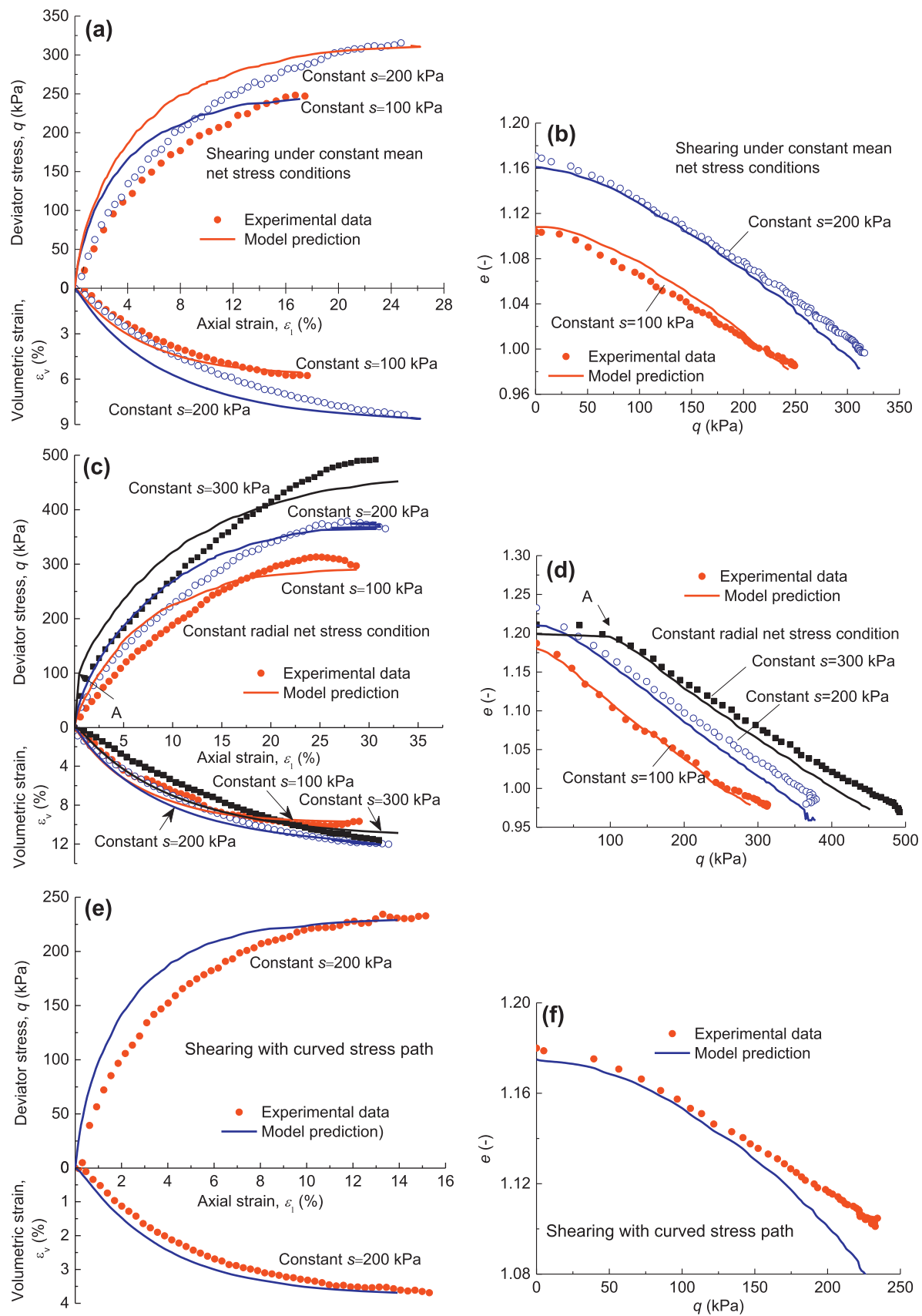


Fig. 12. Comparison between experimental data and model predictions during shearing (data from [51]): (a) and (b) constant mean net stress condition; (c) and (d) constant radial net stress condition; (e) and (f) curved stress path; (g) stress path of shearing test at constant suction of 300 kPa under constant radial net stress; (left side) (a, c, e) deviator stress–axial strain; (right side) (b, d, f) void ratio–deviator stress.

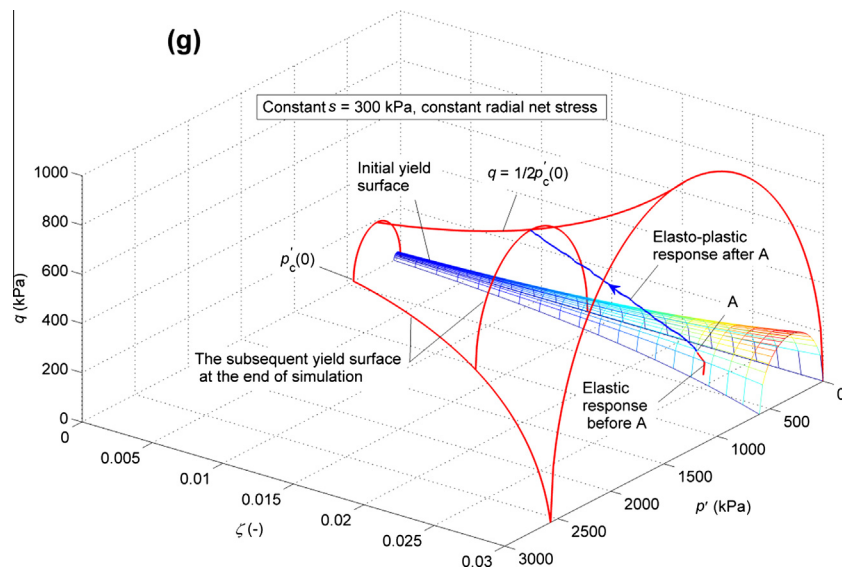


Fig. 12 (continued)

Table 5
Experimental and predicted values of deviator stress at the end of shearing [51].

Test conditions	Suction (kPa)	Deviator stress, q (kPa)		
		Experiment	Model	Error (%)
Constant mean net stress	100	251	243	0.3
	200	315	309	0.2
Constant radial net stress	100	312	288	7.7
	200	379	368	3.0
	300	490	452	7.8
Curved stress path	200	234	229	2.1

Table 6
Soil parameters for shearing tests [45].

Parameter	Value
M	0.720
N	1.520
λ	0.130
κ	0.020
a	6.143
b	0.812
$p'_c(0)$	15.0 kPa
G	3.0×10^3 MPa

isotropic tests A12 ($s = 1$ kPa), A6 ($s = 50$ kPa), A1 ($s = 150$ kPa), A11 ($s = 300$ kPa), and A3 ($s = 350$ kPa), as listed in Table 6. The comparisons between simulations and experiments presented in this section refer to tests B4 and B6 (Fig. 13) that were not used during model calibration. The corresponding simulations are therefore classified as “model predictions”. Note that, in this case, the initial predicted values of void ratio were taken to coincide with the initial experimental values.

5.4.1. Isotropic loading with shearing

Fig. 14 compares experimental and predicted results for Test B4 involving isotropic loading (AB) and shearing (BH) under a constant suction of 300 kPa. The predictions from the Barcelona Basic Model (BBM) [11] and the Wheeler Model (WM) [17] (taken from Raveendiraraj [45]) are also presented in Fig. 14 for comparison purposes. All models seem able to capture the overall trend of the observed mechanical behavior.

During isotropic loading (AB), the void ratio reduced slightly (Fig. 14b). The sample experienced elastic compression until the initial yield stress A' ($p_{net} = 59.28$ kPa). After that, an irreversible change in void ratio occurred ($A'B$). During isotropic loading (AB), the predicted void ratio from BBM is smaller than the experimental data, while the predictions from both WM and the proposed model agree better with the experiments. During shearing (BH), the prediction of void ratio from the proposed model agrees better with the experiments than the other two models, although all models predict smaller values of void ratio than the experiments.

After reaching A' , plastic straining started to occur and continued during the entire shearing stage (BH) until the slope of the

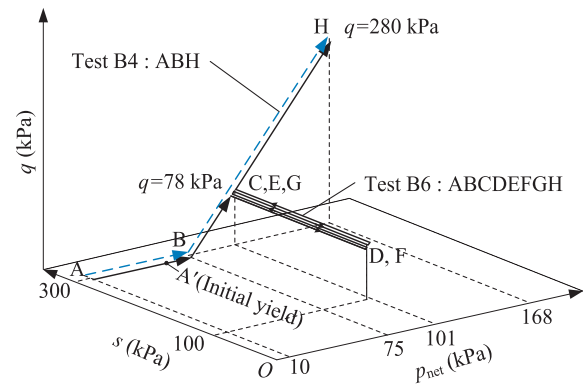


Fig. 13. Stress paths of tests B4 and B6 (from [45]).

stress–strain curves in the q – p_{net} and ϵ_v – ϵ_s planes approached zero as the samples attained critical state at the end of shearing. The variations of predicted volumetric strain with the axial strain are plotted together with the predicted stress–strain curve in Fig. 14. The predicted deviator stress q and ϵ_v do not exactly reach their ultimate values even at the end of simulations. The reason is that the ultimate q value is sensitive to the end point of the simulation. In the corresponding laboratory tests, the critical state is unstable and difficult to control. Nevertheless, our prediction is close to the measurements for the Test B4 within the range of measured q values. With respect to the shearing strain, our prediction results are close to the observations.

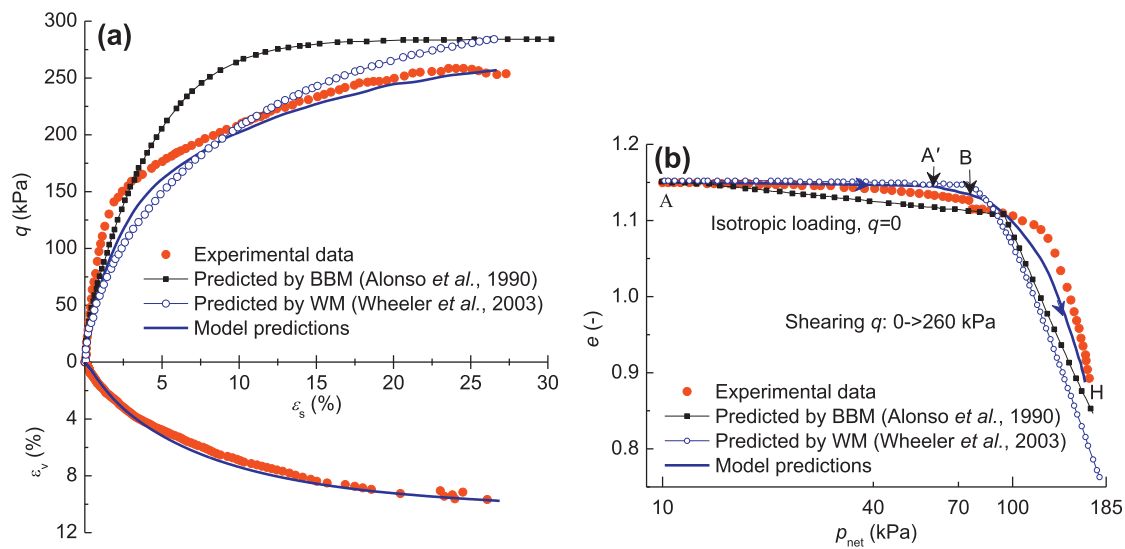


Fig. 14. Comparisons between experimental data and model predictions for Test B4 (data from [45]): (a) deviator stress–shear strain; (b) void ratio–mean net stress.

5.4.2. Isotropic loading with shearing and wetting–drying cycles

Fig. 13 shows the stress path of Test B6 involving shearing under a constant suction of 300 kPa and wetting–drying cycles at constant net stress. The sample was first isotropically loaded to point B and then sheared to point C (corresponding to $p_{net} = 101$ kPa, $q = 78$ kPa and $s = 300$ kPa). After that, it experienced two wetting–drying cycles, with suction varying between 300 and 100 kPa (CD, DE, EF, and FG) while deviator stress and mean net stress remained unchanged.

Fig. 15a and b compare observed and predicted shear strains during shearing and the wetting–drying cycles. Fig. 15a shows that, during the first shearing stage (BC), the predictions from all three models agree very well with experimental data.

The variation of shear strain (ε_s) with suction during the wetting–drying cycles is plotted in Fig. 15b. The experimental values of shear strain increased gradually (with suction decreasing) during the first wetting stage CD, and remained approximately unchanged during the subsequent wetting/drying stages (DE, EF, and FG). This is because, at the beginning of wetting, the stress state (corresponding to point C) laid on the yield surface and plastic collapse therefore occurred during the first wetting. During the subsequent wetting/drying stages, the stress path remained inside the yield surface, with no plastic strains occurring. Furthermore, Fig. 15b and d show that the variation of ε_s during the wetting/drying stages DE, EF and FG is completely reversible, whereas the variation of e is not. This is because during the three elastic loading paths (DE, EF and FG), the elastic shear strain only depends on the deviator stress (see Eq. (34)) which remains unchanged, whereas the void ratio is governed by the mean average skeleton stress p' which depends on degree of saturation and therefore changes in a non-reversible way during the wetting/drying cycles (as shown in Fig. 15e). Overall, with respect to the variation of shear strain with suction, Fig. 15b shows that all models predict with similar accuracy the soil behavior during the wetting–drying cycles but, during the first wetting stage, the proposed model yields slightly better predictions than BBM and WM. As stated by Alonso et al. [11], Eichenberger et al. [52] and Hu et al. [53], the stress path CD is close to the conditions experienced by the soil during rainfall-induced slope failures. Thus the satisfactory prediction of the soil response during this stress path increases the potential of the proposed model for practical applications to geotechnical problems associated with rainfall effects.

After the wetting–drying cycles, the sample was further sheared until it approached critical state. As shown in Fig. 15a, during the entire shearing stage GH, the curve predicted by BBM lies above the experimental one; conversely, the curve predicted by WM lies below the experimental one at the beginning of shearing, but then tends to converge towards the experimental data during the later stage of shearing ($q > 205$ kPa). The predictions by the proposed model agree well with the observations, and the predicted volumetric strain approaches the ultimate critical state value at the end of the simulation. Similar to Test B4, the predicted deviator stress q and ε_v do not exactly reach their ultimate values even at the end of simulations. Nevertheless, the proposed model is able to capture the shearing behavior of unsaturated soils with complex loading stages; even the predicted curve is slightly lower than the observed one at the range of measured q values.

Fig. 15c shows that the void ratio decreased slightly during isotropic loading (AB), with irreversible changes occurring after the yield point A'. A modest reduction of void ratio occurred during the first shearing stage (BC) followed by a larger decrease caused by plastic collapse during the first wetting stage (CD) as shown in Fig. 15d. Void ratio decreased only slightly during the subsequent wetting/drying cycles (DE, EF, and FG). All models capture relatively well the overall trend of the void ratio evolution. However, the present model provides better predictions than other models, especially during stages BC and CD. As shown in Fig. 15d, the values of void ratio predicted by BBM and WM are lower than the corresponding experimental values over the entire wetting–drying stages, resulting also in lower values of void ratio during subsequent shearing. Recall that the present model uses experimental values of degree of saturation for simulating the mechanical response of the soil while the WM predicts degree of saturation together with mechanical behavior. This might have given an advantage to the former model compared to the latter one.

Comparison of tests B6 and B4 indicates that the wetting–drying cycles have a significant effect on the stress–strain relationship. During the first wetting stage, plastic collapse produces additional plastic shear strains and irreversible changes in void ratio. The stress–strain curve and the variation of void ratio of tests B6 and B4 tend however to coincide towards the end of shearing revealing that, as the yield curve continues to expand, the influence of wetting–drying cycles becomes less significant as also stated by Wheeler et al. [17] for isotropic stress states.

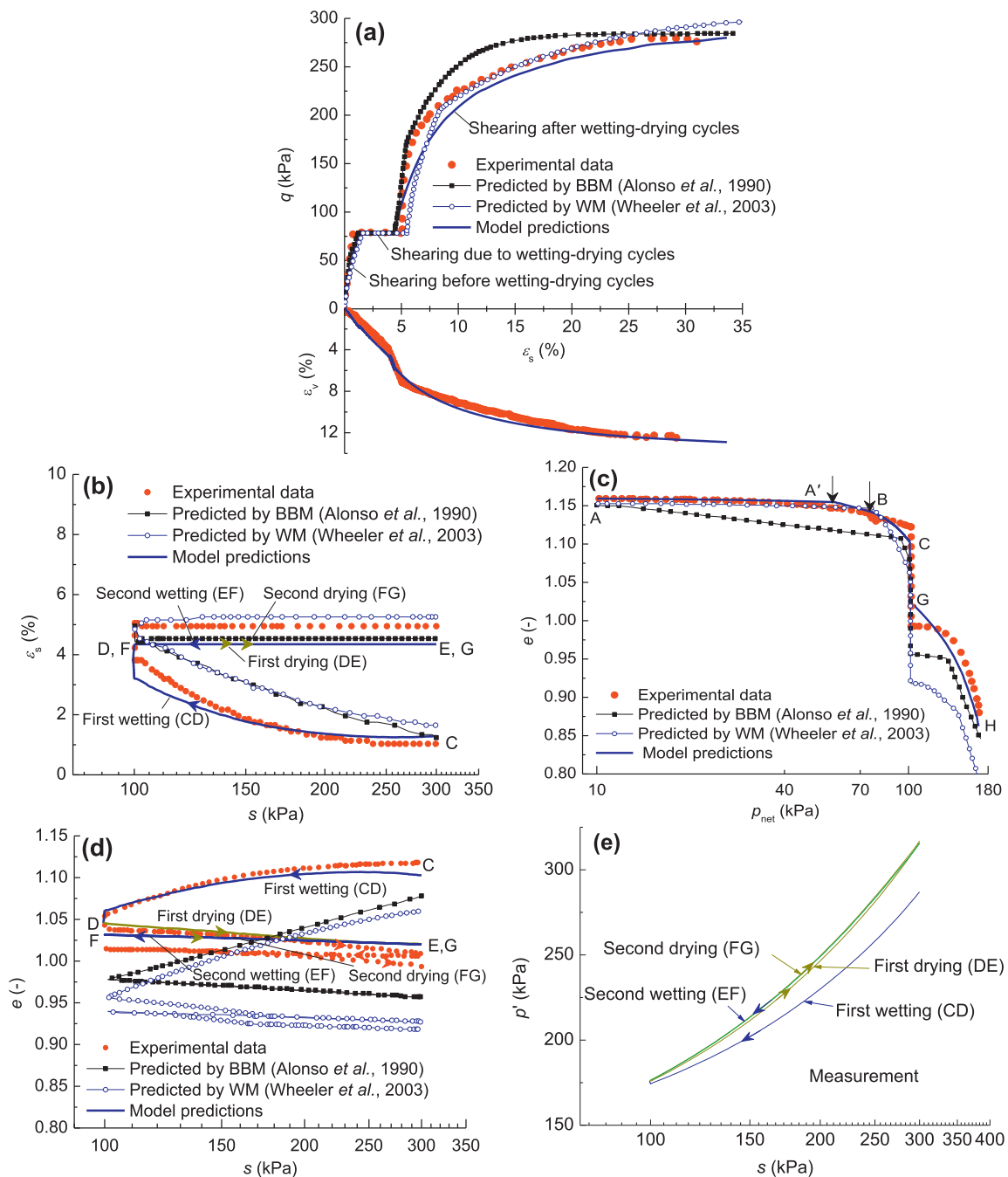


Fig. 15. Comparisons between experimental data and model predictions for Test B6 (data from [45]): (a) deviator stress–shear strain; (b) shear strain–suction; (c) void ratio–mean net stress; (d) void ratio–suction; (e) mean average skeleton stress–suction.

6. Conclusions

A physically based constitutive model for unsaturated soils has been proposed. The bonding factor ζ (representing the magnitude of the inter-particle bonding due to water menisci) and the average skeleton stress are employed as constitutive variables. These variables allow consideration of the effects of the average pore fluid pressure (resulting from pore air and bulk water) and of the inter-particle bonding generated by water menisci. A relationship between e/e_s (i.e. the ratio between unsaturated and saturated values of void ratio at the same average skeleton stress) and the bonding factor ζ has been developed and validated against different experimental data sets. Then an elasto-plastic model has been formulated for both isotropic and triaxial stress states. In the pro-

posed model, only one surface is used to characterize the yield condition of the soil, which also means that a smaller number of model parameters is necessary. Comparisons between simulated and experimental data suggest that the proposed model is able to predict reasonably well a variety of important features of the mechanical behavior of unsaturated soils.

Acknowledgements

We appreciate the constructive comments on the initial version of this paper from Prof. Scott W. Sloan and the anonymous reviewers. This work is funded by the National Basic Research Program of China (No. 2011CB013500), the Open Research Fund of State Key Laboratory of Geomechanics and Geotechnical Engineering, Insti-

tute of Rock and Soil Mechanics, Chinese Academy of Sciences, under Grant No. Z013004, and the National Natural Science Foundation of China (Nos. 51222903 and 51179136). The effort of the second author is funded by U.S. Department of Energy (Contract No. DE-AC03-76SF00098). The financial support of the European Commission to the last author through funding of the 'Marie Curie' industry-academia partnerships and pathways network MAGIC ('Monitoring systems to Assess Geotechnical Infrastructure subjected to Climatic hazards'– Contract: PIAPP-GA-2012-324426) is gratefully acknowledged.

References

- [1] Kohgo Y, Nakano M, Miyazaki T. Theoretical aspects of constitutive modelling for unsaturated soils. *Soils Found* 1993;33(4):49–63.
- [2] Karube D, Kato S. An ideal unsaturated soil and the Bishop's soil. In: *Proc 13th int conf soil mech found engng*, New Delhi; 1994. p. 43–6.
- [3] Karube D, Kawai K. The role of pore water in the mechanical behavior of unsaturated soils. *Geotech Geol Eng* 2001;19(3):211–41.
- [4] Khalili N, Khabbaz M. A unique relationship of chi for the determination of the shear strength of unsaturated soils. *Geotechnique* 1998;48(5):681–7.
- [5] Khalili N, Geiser F, Blight G. Effective stress in unsaturated soils: review with new evidence. *Int J Geomech* 2004;4(2):115–26.
- [6] Lu N, Likos WJ. Suction stress characteristic curve for unsaturated soil. *ASCE J Geotech Geoenviron Eng* 2006;132(2):131–42.
- [7] Fredlund D, Morgenstern N. Stress state variables for unsaturated soils. *ASCE J Geotech Geoenviron Eng* 1977;103(5):447–66.
- [8] Nuth M, Laloui L. Effective stress concept in unsaturated soils: clarification and validation of a unified framework. *Int J Numer Anal Methods Geomech* 2008;32(7):771–801.
- [9] Aitchison G, Donald I. Some preliminary studies of unsaturated soils. (b) Effective stresses in unsaturated soils. In: *Proc 2nd Atstr-N Zealand conf soil mech fnd engng*, Christchurch; 1956. p. 192–9.
- [10] Bishop A, Blight G. Some aspects of effective stress in saturated and partly saturated soils. *Géotechnique* 1963;13(3):177–97.
- [11] Alonso E, Gens A, Josa A. A constitutive model for partially saturated soils. *Géotechnique* 1990;40(3):405–30.
- [12] Wheeler S, Sivakumar V. An elasto-plastic critical state framework for unsaturated soil. *Géotechnique* 1995;45(1):35–53.
- [13] Sun D, Matsuoka H, Yao Y, Ichihara W. An elasto-plastic model for unsaturated soil in three-dimensional stresses. *Soils Found* 2000;40(3):17–28.
- [14] Loret B, Khalili N. An effective stress elastic–plastic model for unsaturated porous media. *Mech Mater* 2002;34(2):97–116.
- [15] Wheeler S. Inclusion of specific water volume within an elasto-plastic model for unsaturated soil. *Can Geotech J* 1996;33(1):42–57.
- [16] Vaunat J, Romero E, Jommi C. An elastoplastic hydromechanical model for unsaturated soils. In *Proceedings of the international workshop on unsaturated soils*, Trento; 2000. p. 121–38.
- [17] Wheeler S, Sharma R, Buisson M. Coupling of hydraulic hysteresis and stress–strain behaviour in unsaturated soils. *Géotechnique* 2003;53(1):41–54.
- [18] Sheng D, Sloan S, Gens A. A constitutive model for unsaturated soils: thermomechanical and computational aspects. *Comput Mech* 2004;33(6):453–65.
- [19] Santagiuliana R, Schrefler B. Enhancing the Bolzon–Schrefler–Zienkiewicz constitutive model for partially saturated soil. *Transport Porous Med* 2006;65(1):1–30.
- [20] Sun D, Sheng D, Sloan S. Elastoplastic modelling of hydraulic and stress–strain behaviour of unsaturated soils. *Mech Mater* 2007;39(3):212–21.
- [21] Romero E, Jommi C. An insight into the role of hydraulic history on the volume changes of anisotropic clayey soils. *Water Resour Res* 2008;44(12):W12412.
- [22] Sheng D, Fredlund D, Gens A. A new modelling approach for unsaturated soils using independent stress variables. *Can Geotech J* 2008;45(4):511–34.
- [23] Buscarnera G, Nova R. An elastoplastic strainhardening model for soil allowing for hydraulic bonding–debonding effects. *Int J Numer Anal Methods Geomech* 2009;33(8):1055–86.
- [24] Zhou A, Sheng D, Sloan S, Gens A. Interpretation of unsaturated soil behaviour in the stress–saturation space, I: volume change and water retention behaviour. *Comput Geotech* 2012;43:178–87.
- [25] Gallipoli D, Gens A, Sharma R, Vaunat J. An elasto-plastic model for unsaturated soil incorporating the effects of suction and degree of saturation on mechanical behaviour. *Géotechnique* 2003;53(1):123–36.
- [26] Gallipoli D, Gens A, Chen G, D'Onza F. Modelling unsaturated soil behaviour during normal consolidation and at critical state. *Comput Geotech* 2008;35(6):825–34.
- [27] Haines W. A note on the cohesion developed by capillary forces in an ideal soil. *J Agric Sci* 1925;15(4):529–43.
- [28] Likos W, Lu N. Hysteresis of capillary stress in unsaturated granular soil. *J Eng Mech ASCE* 2004;130(6):646–55.
- [29] Cho G, Santamarina J. Unsaturated particulate materials–particle-level studies. *J Geotech Geoenviron Eng* 2001;127(1):84–96.
- [30] Mitarai N, Nori F. Wet granular materials. *Adv Phys* 2006;55(1–2):1–45.
- [31] Scholtès L, Hicher P, Nicot F, Chareyre B, Darve F. On the capillary stress tensor in wet granular materials. *Int J Numer Anal Methods Geomech* 2009;33(10):1289–313.
- [32] Fleureau J, Hadiwardoyo S, Correia A. Generalised effective stress analysis of strength and small strains behaviour of a silty sand, from dry to saturated state. *Soils Found* 2003;43(4):21–33.
- [33] Willson CS, Ning L, Likos WJ. Quantification of grain, pore, and fluid microstructure of unsaturated sand from X-ray computed tomography images. *ASTM Geotech Test J* 2012;35(6):911–23.
- [34] Likos WJ, Jaafar R. Pore-scale model for water retention and fluid partitioning of partially saturated granular soil. *ASCE J Geotech Geoenviron Eng* 2013;139(5):724–37.
- [35] Justo J, Vázquez M. A model for capillary pressure in unsaturated granular soils within the pendular saturation regime. In: Alonso EE, Gens A, editors. *Unsaturated soils*, vol. 3. CRC Press; 2011. p. 151–6.
- [36] Lewis R, Schrefler B. *The finite element method in the static and dynamic deformation and consolidation of porous media*. Chichester: Wiley; 1998.
- [37] Brooks RH, Corey AT. *Hydraulic properties of porous media*. Hydrology paper no. 3. Fort Collins, CO, USA; 1964.
- [38] van Genuchten MT. A closed-form equation for predicting the hydraulic conductivity of unsaturated soils. *Soil Sci Soc Am J* 1980;44(5):892–8.
- [39] Bishop A. The principle of effective stress. *Tek Ukeblad* 1959;39:859–63.
- [40] Jennings J, Burland J. Limitation to the use of effective stress in partially saturated soils. *Géotechnique* 1962;12(2):125–44.
- [41] Toll D. A framework for unsaturated soil behaviour. *Géotechnique* 1990;40(1):31–44.
- [42] Sivakumar V. A critical state framework for unsaturated soil. Ph.D. thesis. UK: University of Sheffield; 1993.
- [43] Sharma R. Mechanical behaviour of unsaturated highly expansive clays. Ph.D. thesis. UK: University of Oxford; 1998.
- [44] Barrera M. Estudio experimental del comportamiento hidro-mecánico de suelos colapsables. Thesis doctoral. Spain: Universitat Politècnica de Catalunya; 2002.
- [45] Raveendraraj A. Coupling of mechanical behaviour and water retention behaviour in unsaturated soils. Ph.D. thesis. UK: University of Glasgow; 2009.
- [46] Gallipoli D, Toll D, Augarde C, Tarantino A, De Gennaro V, Vaunat J, et al. The MUSE network: sharing research expertise on unsaturated soils across Europe. In: *4th International conference on unsaturated soils*, Arizona; 2006. p. 2075–85.
- [47] Roscoe K, Burland J. On the generalized stress–strain behaviour of wet clay. *Eng Plast* 1968;3:539–609.
- [48] Jaky J. Pressure in silos. In: *Proc 2nd int conf soil mech and fnd engng*, Rotterdam; 1948. p. 103–7.
- [49] Gallipoli D. A hysteretic soil–water retention model accounting for cyclic variations of suction and void ratio. *Géotechnique* 2012;62(7):605–16.
- [50] Hu R, Chen Y-F, Liu H-H, Zhou C-B. A water retention curve and unsaturated hydraulic conductivity model for deformable soils: consideration of the change in pore size distribution. *Géotechnique* 2013;63(16):1389–405.
- [51] Sivakumar R. Effects of anisotropy on the behaviour of unsaturated compacted clay. Ph.D. thesis. UK: The Queen's University of Belfast; 2005.
- [52] Eichenberger J, Nuth M, Laloui L. Modeling landslides in partially saturated slopes subjected to rainfall infiltration. *Mech Unsaturat Geomater* 2010:233–50.
- [53] Hu R, Chen Y, Zhou C. Modeling of coupled deformation, water flow and gas transport in soil slopes subjected to rain infiltration. *Sci China Tech Sci* 2011;54(10):2561–75.